Int. J. Electrochem. Sci., 11 **(2016)** 3591 - 3603

International Journal of
ELECTROCHEMICAL
SCIENCE
www.electrochemsci.org

Electrospun Sn Embedded in Carbon Nanofibers as an Anode for High-Performance Lithium-Ion Batteries

Da-Mi Kim, Young-Woo Lee, Si-Jin Kim, Min-Cheol Kim, Gyu-Ho Lee, Hui-Seon Choe, Wansoo Huh and Kyung-Won Park[*]

Department of Chemical Engineering, Soongsil University, Seoul 156743, Republic of Korea
[*]E-mail: kwpark@ssu.ac.kr

Received: 4 February 2016 / *Accepted:* 13 March 2016 / *Published:* 1 April 2016

Well-defined composite electrodes have been known to have enhanced lithium ion reaction such as the capacity, stability, and cycling performance. We prepared the composite electrodes consisting of Sn nanoparticles and carbon nanofibers (Sn/CNF) as an anode material for high-performance lithium-ion batteries (LIBs) using electrospinning method and calcination process under nitrogen atmosphere. The as-prepared Sn/CNF showed metallic Sn nanoparticles uniformly embedded in the CNF as confirmed by X-ray diffraction (XRD), raman spectroscopy, X-ray photoelectron spectroscopy (XPS), field-emission scanning electron microscopy (FE-SEM), energy-dispersive X-ray spectroscopy (EDX), and field-emission transmission electron microscopy (FE-TEM). The performance of the samples as an anode for LIBs was evaluated by charge-discharge and high rate curves, cyclic voltammograms (CVs), and electrochemical impedance spectroscopy using lithium coin cells. Compared to CNF-only, Sn/CNF exhibited high specific capacity, improved stability, and excellent high rate cycling performance due to low transport resistance and high diffusion coefficient for lithium ions.

Keywords: composite materials; nanostructures; electrochemical properties

1. INTRODUCTION

Rechargeable lithium-ion batteries (LIBs) have been extensively utilized as an electrochemical power source of portable electronics and electric vehicle with essential requirements such as high durability, high-energy density, and improved safety [1, 2]. Especially, for an extremely improved performance of LIBs, the development of higher capacity anode materials should be proposed compared with the commercial graphite as an anode with a theoretical capacity of ~372 mAh g^{-1} [3, 4]. Recently, metals and semiconductors, i.e., Sn, Ge, and Si, electrochemically react with lithium to form alloys with a large number of lithium atoms, thus providing a high specific capacity [5-8]. Among

doi: 10.20964/110441

these materials, the Li–Sn alloy has a theoretical specific capacity of ~994 mAh g^{-1}, with a fully lithiated composition of $Li_{4.4}Sn$ as follows [9-13]:

$Sn + xLi^+ + 4e^- \leftrightarrow Li_xSn$ ($0<x\leq4.4$)

However, Sn-based anode materials, despite of its high theoretical capacity, exhibit poor electrochemical performance of LIBs during the lithium alloying/dealloying process in the anodes because of the pulverization caused by the large volume change, particle aggregation, and unstable solid electrolyte interphase, thus resulting in serious capacity fading [14-18].

To overcome these issues for high-performance LIBs, composite structure electrodes based on one-dimensional (1-D) carbon matrix including nanowires, nanotubes, and nanofibers have been developed and proposed in the literatures [19, 20]. In the carbon composite electrodes, 1-D carbon can suppress Sn particle aggregation and support electrochemical active sites for charge-transfer reactions [21, 22] due to its high electrical conductivity, good chemical stability, and light-weight nature for the energy storage devices [23]. Especially, it is reported that the electrospinning is a well-known, simple, inexpensive, and scalable technique, which has received much attention in the preparation of 1-D nanomaterials [24-27]. The electrospun carbon nanofibers (CNF) can be formed with submicrometer diameters, with particular functionalities, and having high surface-to-volume ratios [28]. Moreover, the electrochemical performance for the CNF-based anodes might be affected by their surface functional groups with non-carbon elements such as nitrogen, boron, and phosphorous [29-32]. The presence of chemical dopants at the carbon surface can enhance the reactivity and electric conductivity, and hence the Li-ion storage performance [33-35]. It is expected that the nanocomposite anode consisting of Sn and CNF (Sn/CNF) can result in higher interfacial areas, shorter path lengths for Li-ion transport, and accommodation of the strain of lithium insertion/desertion [36, 37].

Herein, we prepared the Sn/CNF composites as an anode for high-performance LIBs using electrospinning and calcination process. The structural and chemical analysis of the as-prepared samples was characterized using field-emission transmission electron microscopy (FE-TEM), field-emission scanning electron microscopy (FE-SEM), energy-dispersive X-ray spectroscopy (EDX), X-ray diffraction (XRD), and X-ray photoelectron spectroscopy (XPS). To characterize the performance of the samples as an anode for LIBs, the charge-discharge and high rate curves, cyclic voltammograms (CVs), and electrochemical impedance spectroscopy of the electrodes were obtained using lithium coin cells.

2. EXPERIMENTAL SECTION

2.1 Fabrication of Sn/CNF

The precursor solution was prepared by dissolving 10 wt.% polyacrylonitrile (PAN, $(C_3H_3N)_n$, Mw = 150,000 g mol^{-1}, Aldrich, 99.99%) in N,N-dimethylformamide (DMF, $HCON(CH_3)_2$, Aldrich, 99.8 %). In order to control the amount of metallic Sn and C, the ratios between PAN and $SnCl_4 \cdot 5H_2O$ in the precursor solution for the electrospinning process were changed from 1:0.5 to 1:1 (denoted as Sn/CNF-0.5 and Sn/CNF-1, respectively). For comparison, the precursor solution of 10 wt.% PAN in

DMF was prepared to fabricate CNF without Sn (denoted as CNF-only). The precursor solution was loaded into a plastic syringe connected to a blunt-tip needle, which was connected to a syringe pump. The distance between the tip and Al collector was 15 cm. The electrospinning process was then carried out with a high voltage (17 kV) linked to the needle tip of a syringe offering the well-prepared solution at a flow rate of 15 μL min^{-1}. The electrospun fibers were dried in an oven at 60 ^{o}C for 24 h and then carbonized in a tube furnace at 800 ^{o}C for 3 h under a nitrogen atmosphere with a heating rate of 10 $^{\circ}$C min^{-1} in order to obtain the Sn/CNF composite electrodes.

2.2 Characterization of the as-prepared Sn/CNF

The crystal structure was studied using an XRD (D2 PHASER, Bruker AXS) with a Cu K_{α} (λ = 0.15418 nm) source with a nickel filter. The source was operated at 30 kV and 10 mA. The 2θ angular scan from 10° to 80° was explored at a scan rate of 0.5° min^{-1}. Raman spectra were recorded on a high resolution micro raman spectrometer (Horiba Jobin Yvon, LabRAM HR UV/Vis/NIR PL). XPS (Thermo VG, U.K.) analysis was carried out with an Al K_{α} X-ray source of 1486.6 eV at a chamber pressure below 1×10^{-8} Torr and a beam power of 200 W. All high resolution spectra were collected using pass energy of 46.95 eV. The step size and time per step were set at 0.025 eV and 100 ms, respectively. TGA curves were obtained in a thermal analyzer (SDTA851, Mettler Toledo) in the range of 25-900 ^{o}C at a heating rate of 5 ^{o}C min^{-1} under an air flow of 60 cm^{3} min^{-1}. The size and morphology of the as-prepared samples were observed on a FE-SEM (JSM-6700F, JEOL Ltd.) and a FE-TEM (Tecnai G2 F30 system operating at 300 kV).

2.3 Electrochemical characterization of Sn/CNF electrodes

To assemble the coin cells (size 2032, Hohsen Corporation), the composite electrodes were used as a working electrode and evaluated with respect to a lithium foil (FMC Corporation) as a counter/reference electrode. The as-synthesized Sn/CNF composite as an active material, ketjen black as a conducting material (Alfa Aesar), and polyvinylidene difluoride (Alfa Aesar) as a binder with a weight ratio of 70:10:20 were mixed in 1-methyl-2-pyrrolidinone solvent (Aldrich, 99%). The well-mixed slurry was coated onto a Cu foil as a current collector using a doctor blade technique and then dried in an air atmosphere at 100 ^{o}C for 12 h. The average loading amount of active materials for all electrodes was 0.5~0.6 mg cm^{-2}. All of the Sn/CNF electrodes were uniformly coated on 15 mm thick copper foil substrates. The thickness of the electrodes was 40 ~ 45 μm after pressing. The coin cells were assembled inside an argon-filled glove box (< 5 ppm, H_2O and O_2). The electrodes of the cells were separated by a porous polypropylene membrane (Celgard 2400) and an electrolyte solution consisting of 1.1 M $LiPF_6$ in (ethylene carbonate:dimethyl carbonate) = (1:1) as a solvent mixture (Techno Semichem Co., Ltd). The charge–discharge cycling was performed within the voltage range of 0–3.0 V vs. Li/Li^{+} on a battery test instrument (PEBC 50.2 PnE Solution Co., Ltd) under constant temperature of 25 ^{o}C. Electrochemical impedance spectroscopy measurements (EIS) were performed on the AUTOLAB electrochemical workstation by applying an AC voltage of 5 mV amplitude over

the frequency range 100 kHz–0.01 Hz at open circuit potential. All the measurements were performed at room temperature.

3. RESULTS AND DISCUSSION

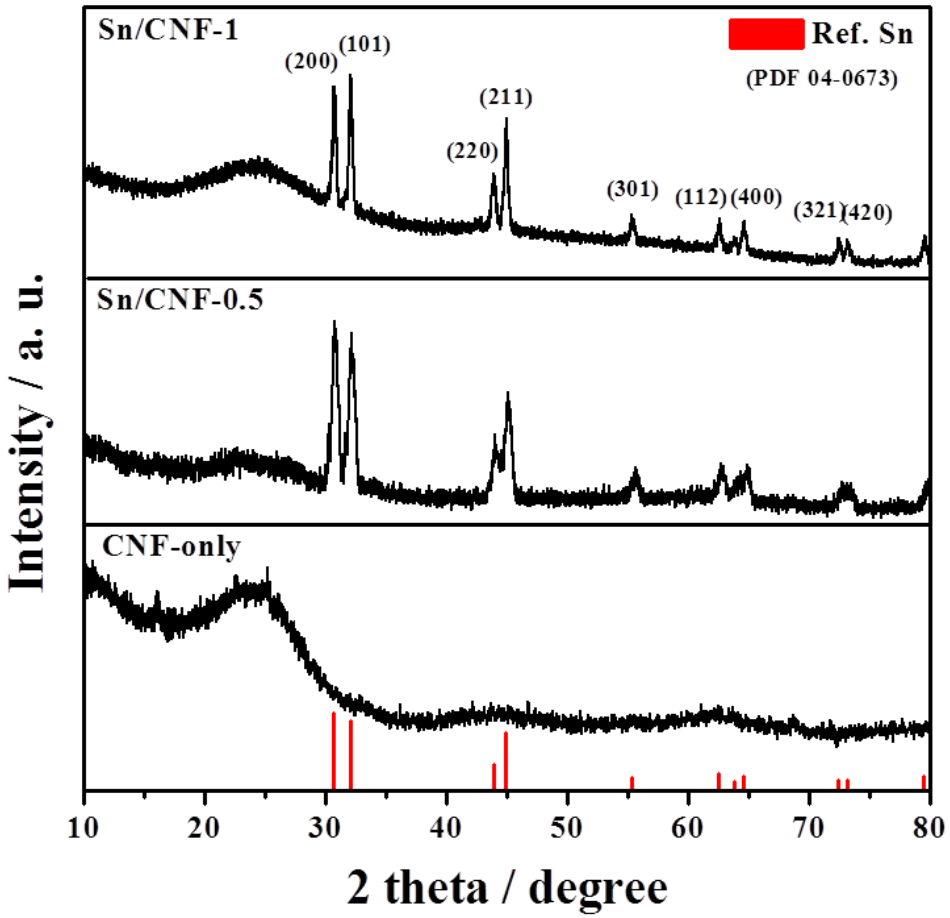

Figure 1. XRD patterns of Sn/CNF-0.5 and Sn/CNF-1 compared with CNF-only.

Figure 1 shows the XRD patterns of Sn/CNF-0.5 and Sn/CNF-1 compared with CNF. The diffraction peaks of Sn/CNF-0.5 and Sn/CNF-1 were in good agreement with the reference data (JCPDS No. 04-0673) for the tetragonal Sn metallic phase with space group I41/amd (141) and no extra peaks related to SnO_2 were observed. The representative diffraction peaks of Sn in the Sn/CNF electrodes were detected at 30.65°, 32.02°, 43.87°, 44.90°, and 55.33° corresponding to (200), (101), (220), (211), and (301) planes. However, the broad diffraction peaks of Sn/CNF-0.5 and Sn/CNF-1 around at $2\theta=25^{o}$ corresponding to (002) plane in the XRD patterns of CNF-only resulted from the formation of CNF.

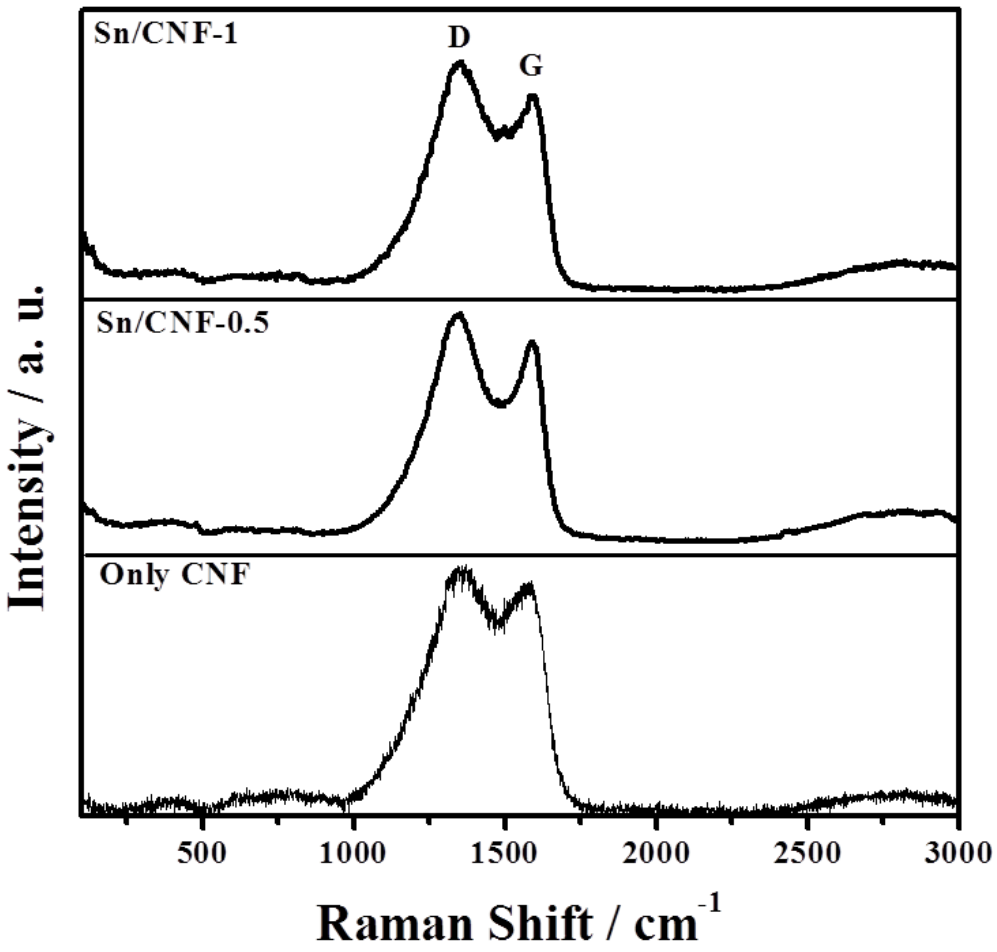

Figure 2. Raman spectra of Sn/CNF-0.5, Sn/CNF-1, and CNF-only

The Raman spectra of Sn/CNF-0.5, Sn/CNF-1, and CNF-only consisted of the two characteristic peaks consist of G and D band at ~1589 and ~1356 cm^{-1}, respectively (Fig. 2). In the Raman spectra, the G band is associated with the E_{2g} vibration mode of sp^2 carbon crystal structures whereas the D band reflect the structural defects and partially disordered structures on the graphitic plane, which might be as a result of doping of heteroatoms, vacancies, grain boundaries or other defects [38].

The relative intensity ratio (I_D/I_G) values, i.e. degree of structural disorder of Sn/CNF-0.5, Sn/CNF-1, and CNF-only were 1.12, 1.14 and 1.08, respectively. The increased I_D/I_G ratio is attributed to the structural defects dominantly formed during the pyrolysis process with reduction of Sn ions to nanoparticles in CNF and carbonization process of PAN as CNF and nitrogen dopants sources. The chemical states of as-prepared samples were characterized using XPS analysis (Fig. 3). The wide scans of Sn/CNF-0.5 and Sn/CNF-1 showed the existence of Sn and nitrogen species as well as carbon. The contents of Sn for Sn/CNF-0.5 and Sn/CNF-1 were 2.18 and 5.15 at.%, respectively.

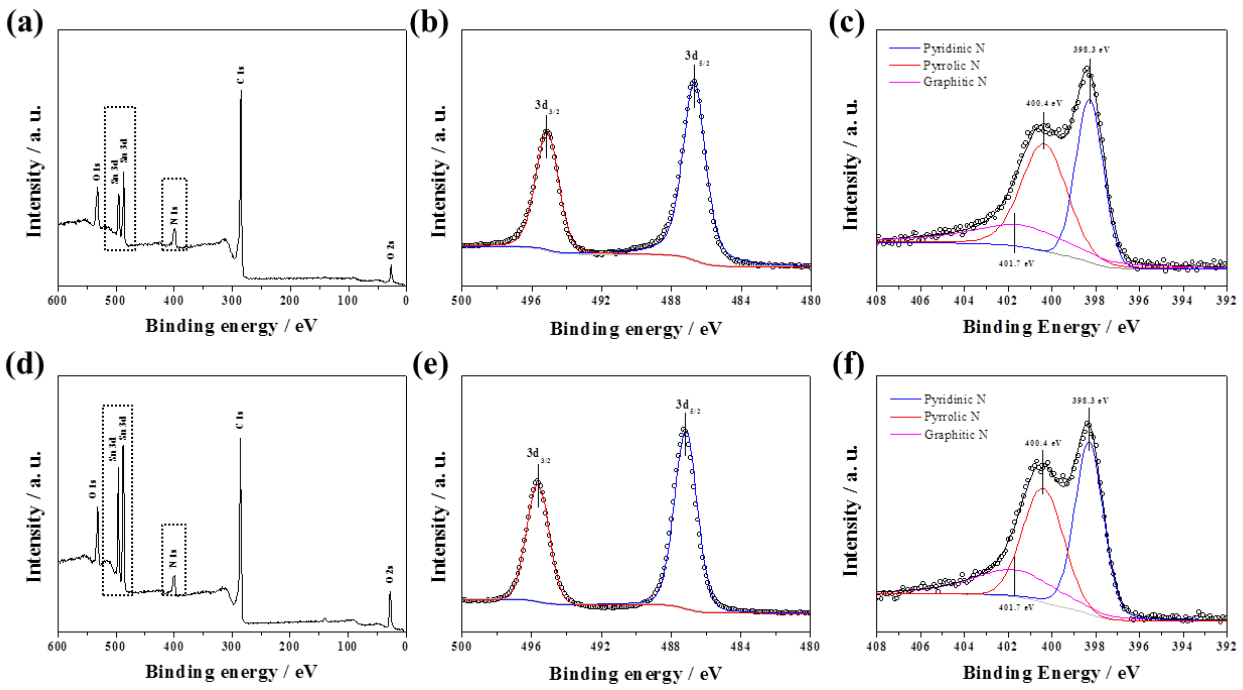

Figure 3. Wide and fine N1s XPS spectra of Sn/CNF-0.5 ((a),(b)) and Sn/CNF-1((c),(d))

Especially, high-resolution N1s spectra of the samples contained specific characteristic curves with binding energies of 398.3, 400.4, and 401.7 eV, corresponding to pyridinic, pyrrolic, and graphitic N, respectively, as shown in Fig. 3(b) and (d). The presence of the chemical dopant such as nitrogen at the carbon surface can enhance the reactivity and electric conductivity, hence leading to high-performance LIBs [39-45]. The ratio of Sn to CNF in the composites was determined using TGA as shown in Fig. 4.

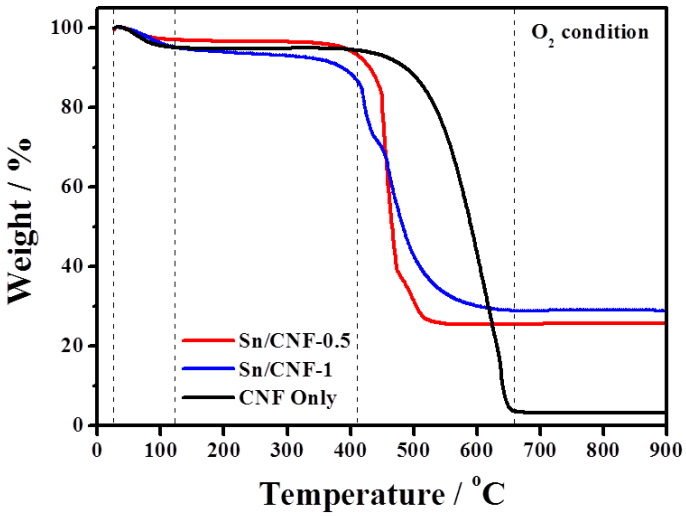

Figure 4. TGA curves of the as-prepared samples

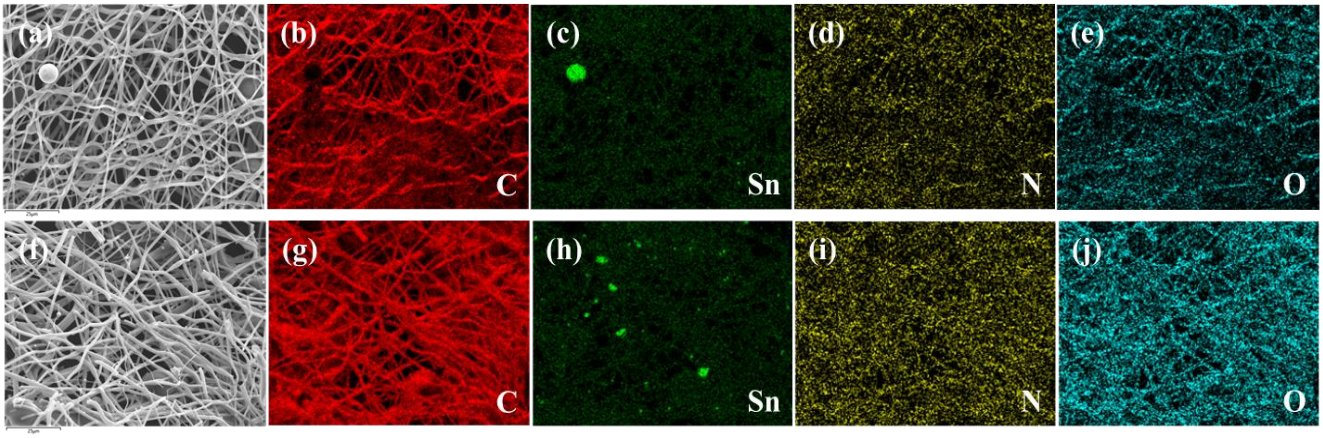

Figure 5. SEM images and mapping images of Sn/CNF-0.5 and Sn/CNF-1

The first weight loss corresponds with the evaporation of water and solvent in the range of 25 ^{o}C to 110 ^{o}C. Almost no weight loss was observed from 110 to 220 °C, demonstrating that the composite is stable up to 220 °C in air, that is, there is no Sn oxidation reaction and carbon decomposition at a temperature of lower than 220 °C. The weight loss around at 400 ^{o}C is mainly due to the oxidation of carbon ($C + O_2 \rightarrow CO_2$) and the subsequent weight gain after 450 ^{o}C is due to the oxidation of Sn NPs ($Sn + O_2 \rightarrow SnO_2$) [10]. The Sn contents in Sn/CNF-0.5 and Sn/CNF-1 were determined to be 20.17 and 23.25 wt.%, respectively.

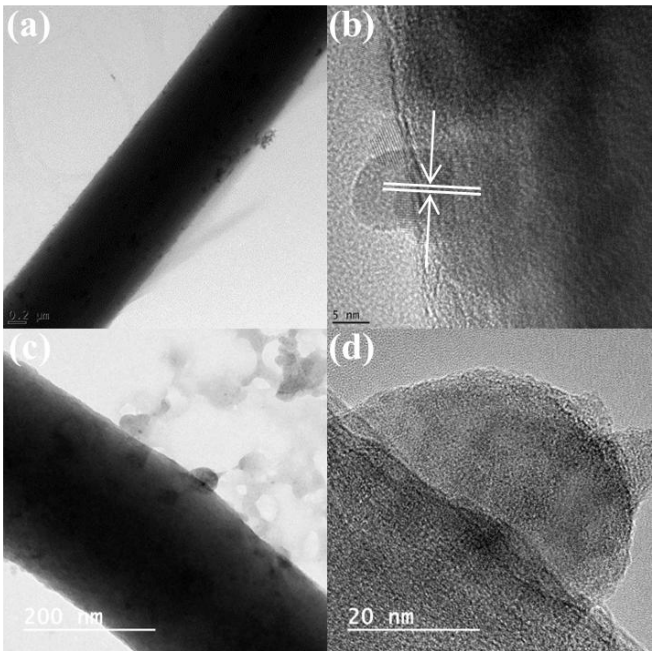

Figure 6. TEM images of Sn/CNF-0.5((a),(b)) and Sn/CNF-1((c),(d))

Fig. 5 shows the SEM images of Sn/CNF-0.5 and Sn/CNF-1 with diameters of 1.0-1.5 um. The composites seem to have a smooth surface and no nanoparticles on the CNF surface, representing most of Sn phases is embedded in the CNFs. In order to identify the elemental distribution of the as-

prepared samples, as shown in Fig. 5(a)-(h), the mapping images for carbon, nitrogen, oxygen, and Sn metal were obtained using SEM-EDX spectroscopy. The Sn NPs were uniformly distributed along the CNFs. The Sn contents for Sn/CNF-0.5 and Sn/CNF-1 were 6.92 and 12.59 wt.%, respectively. Fig. 6 shows the TEM images of Sn/CNF-0.5 and Sn/CNF-1 to investigate the encapsulation of Sn NPs in the CNFs. The Sn NPs with particle sizes ranging from 7 to 19 nm (Avg. 13.82 nm) were well dispersed in the CNFs, exhibiting carbon matrix with separating individual Sn NPs. The high-resolution TEM images of Fig. 6(c) and (d) displays the fine lattice fringe and crystalline nature of a single Sn NP in the CNF.

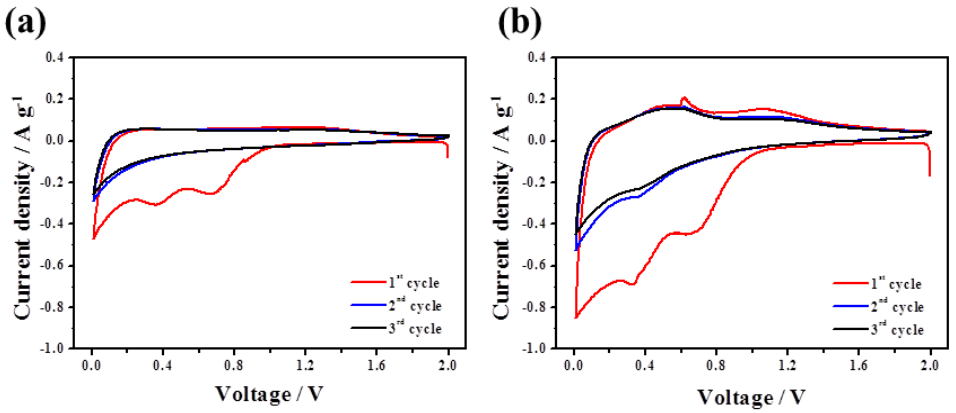

Figure 7. CVs of (a) CNF-only and Sn/CNF-1 obtained from 0.01 to 2.0 V *vs.* Li^+/Li with a scan rate of 0.1 mV s^{-1}

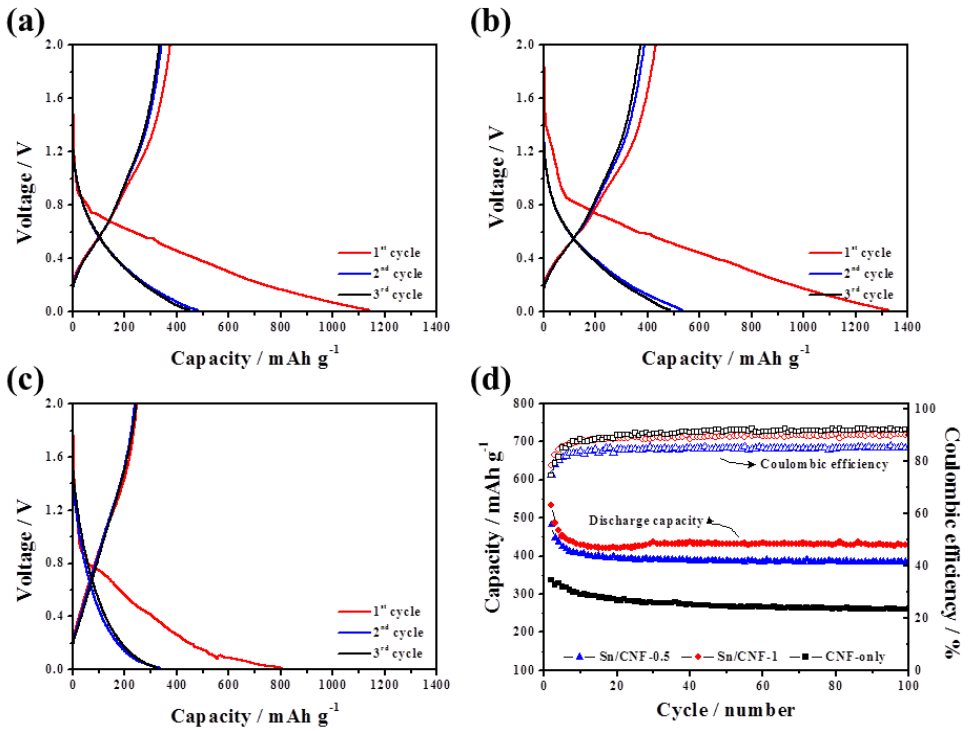

Figure 8. 1st, 2nd, and 3rd discharge/charge profiles for (a) Sn/CNF-0.5, (b) Sn/CNF-1, and (c) CNF-only measured at a current density of 200 mA g^{-1}. Cycling performance and Coulombic efficiency for the samples at a current density of 200 mA g^{-1} for 100 cycles

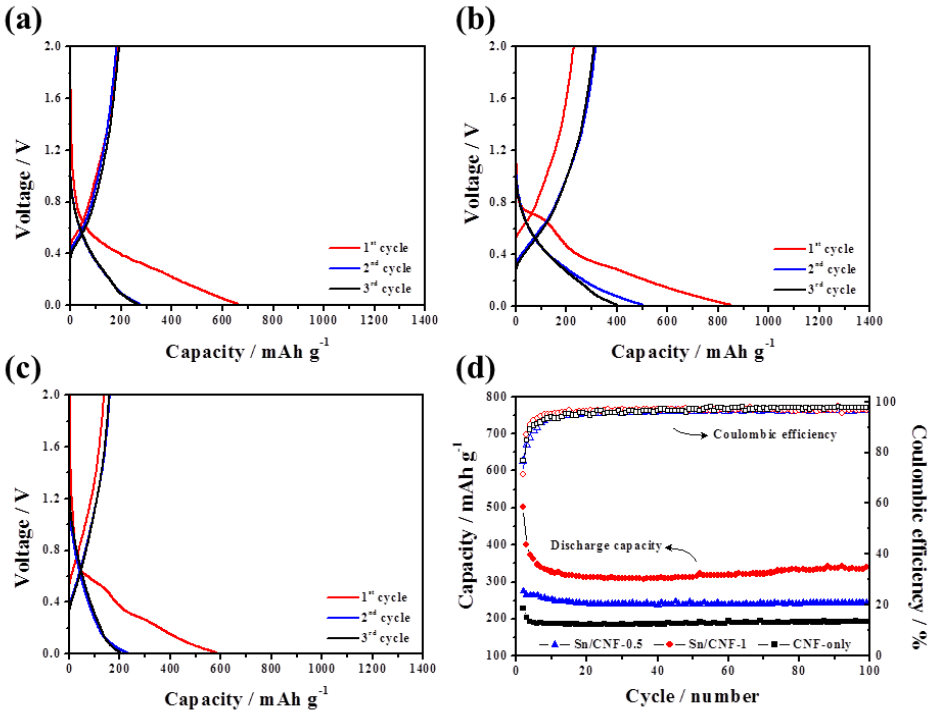

Figure 9. 1st, 2nd, and 3rd discharge/charge profiles for (a) Sn/CNF-0.5, (b) Sn/CNF-1, and (c) CNF-only measured at a current density of 800 mA g^{-1}. Cycling performance and Coulombic efficiency for the samples at a current density of 800 mA g^{-1} for 100 cycles

To further identify the electrochemical properties of the electrodes, CVs of the electrodes were obtained from 0.01 to 2.0 V *vs*. Li^+/Li with a scan rate of 0.1 mV s^{-1}, as shown in Figs. 7(a), 7(b). In the 1st CV curves, the as-prepared electrodes exhibited irreversible reductions due to the formation of a solid-electrolyte interface (SEI) layer. In the subsequent cycles, three small reversible reduction peaks at 0.19, 0.38, and 0.53 V are assigned to the lithium insertion into tin to form a Li_xSn alloy. The deep cathode peak around 0.01 V represents lithium insertion from CNF. The unchanged oxidation peaks at 0.48 and 0.61 V correspond to the desertion reaction of Li_xSn alloy, and the broad anodic peak at 1.1 V represents lithium extraction from carbon [46, 47]. After the first cycle, the distinct cathodic and anodic current curves are well overlapped, suggesting that maintain the structural integrity and a stable electrochemical reaction of Sn/CNF electrode.

Figs. 8(a)-8(c) show the 1st, 2nd, and 3rd discharge/charge profiles for the electrodes measured at a current density of 200 mA g^{-1} with the potential range of 0.01-2.0 V *vs*. Li^+/Li. The first discharge capacities of Sn/CNF-0.5, Sn/CNF-1, and CNF-only were 1142.2, 1131.0, and 804.8 mAh g^{-1}, and the 2nd capacities are 484.9, 534.1, and 335.2 mAh g^{-1}, respectively. In the case of CNF-only, the specific discharge capacity was much lower than other two samples and similar to that of carbonaceous material such as graphite. The Coulomb efficiencies of initial cycles in the electrodes were as follows: Sn/CNF-0.5 (42.45%), Sn/CNF-1 (47.22%), and CNF-only (41.65%). During the initial Li ion charge (insertion) reaction, an obvious voltage plateau at around 0.8 V for Sn/CNF and CNF-only results from the main lithiation reaction of CNF due to the formation of SEI film. In the cycle performance, Sn/CNF-1 exhibited higher capacity retention (429.7 mAh g^{-1}) after 100 cycles compared with Sn/CNF-0.5 and CNF-only (383.6 and 260.4 mAh g^{-1}, respectively). The improved capacity of

Sn/CNF-1 can result in the stable composite structure and fast ionic/electronic diffusion. As shown in Fig. 9, the Sn/CNF electrodes exhibited a improved discharge capacities and superior cycling performance at a current density of 800 mA g^{-1}, delivering a high Coulombic efficiency, which gradually increased from 70% in the first cycle to 99% in the 10^{th} cycles and remained above 99% during the subsequent cycles, indicating that nitrogen in the CNFs can lead to a facile insertion/extraction of lithium ions as well as an improved transport of electrons and ions [39-45].

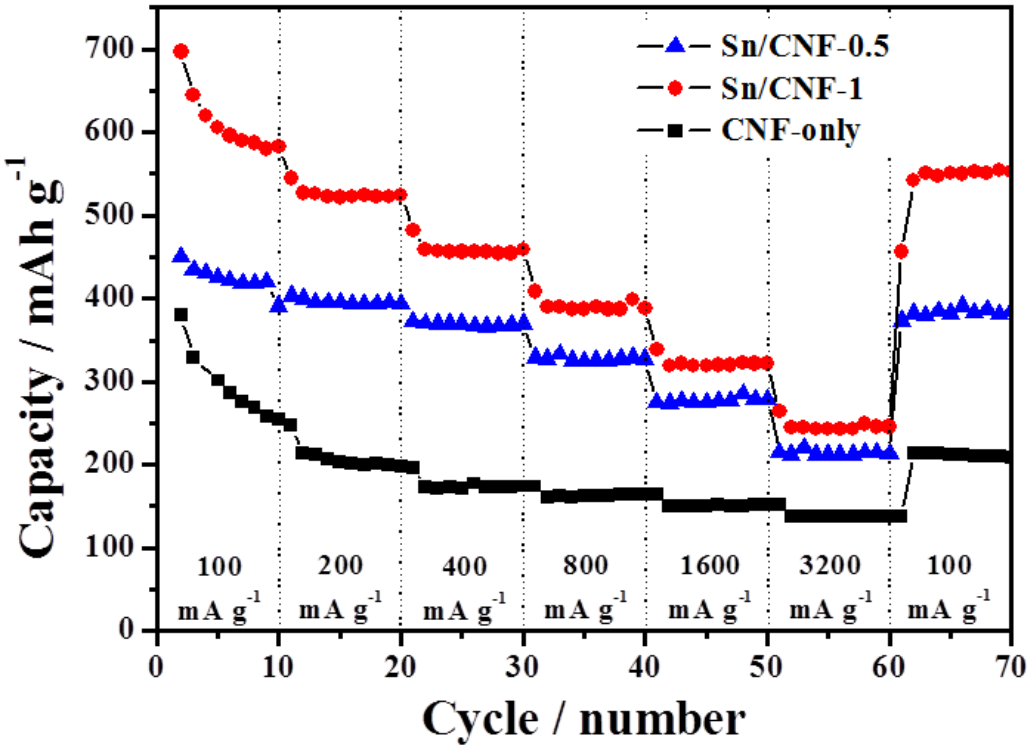

Figure 10. High rate cycling performance of the samples at current densities of 100, 200, 400, 800, 1600, and 3200 mA g^{-1}

To further investigate the electrochemical performance of the electrodes, high rate performance was measured, as indicated in Fig. 10. The discharge capacities of Sn/CNF-0.5 were 424.9, 396.1, 369.6, 324.3, 275.3, and 212.5 mAh g^{-1} at current densities of 100, 200, 400, 800, 1600, and 3200 mA g^{-1}, respectively, and the discharge capacities of Sn/CNF-1 were 605.7, 521.4, 455.7, 387.1, 318.6, and 242.9 mAh g^{-1} at current densities of 100, 200, 400, 800, 1600, and 3200 mA g^{-1}, respectively, and the discharge capacities of CNF-only were 285.7, 201.2, 171.4, 161.9, 151.2, and 136.9 mAh g^{-1} at current densities of 100, 200, 400, 800, 1600, and 3200 mA g^{-1}, respectively. The improved high rate cycling performance at high current densities might be attributed to Sn NPs embedded in the CNFs and 1-D electrode structure facilitating Li-ion transport.

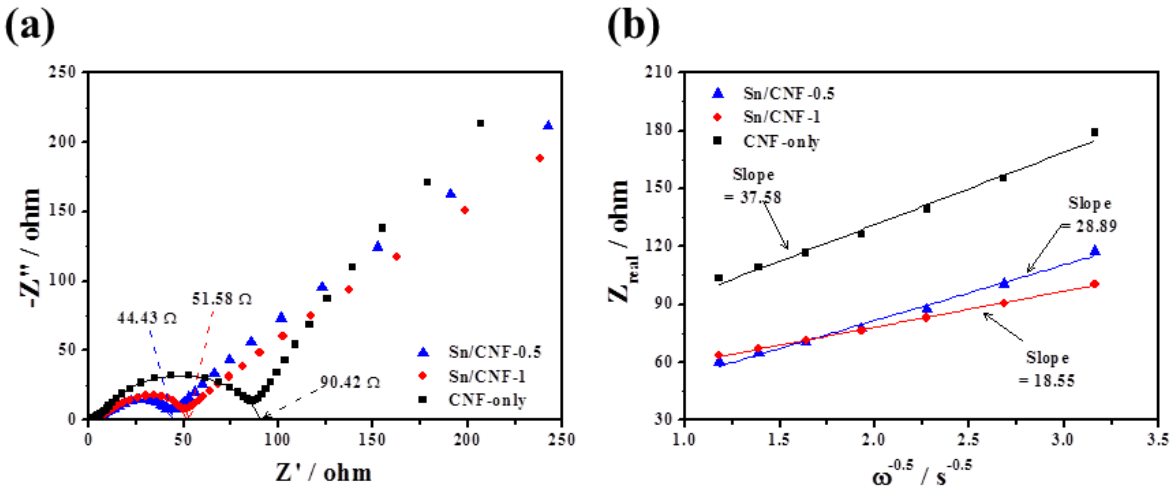

Figure 11. Nyquist plots of the electrodes obtained after 100 cycles at open circuit potential between 100 kHz and 10 mHz

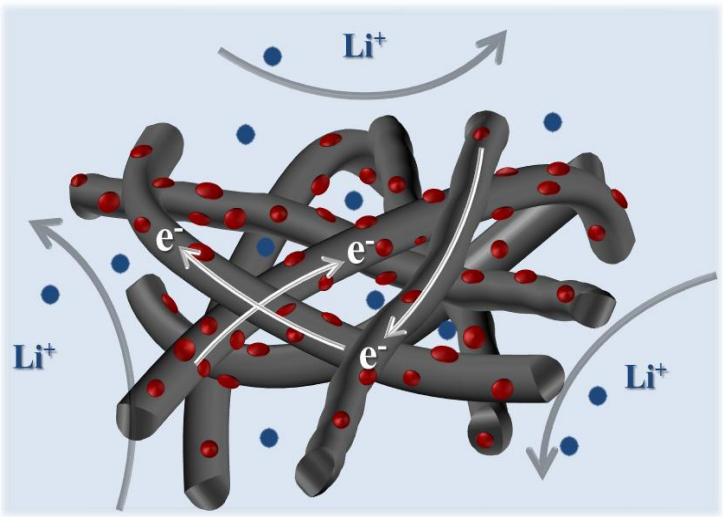

Figure 12. Schematic illustration of Sn/CNF prepared using electrospinning method and calcination process under nitrogen atmosphere.

Fig. 11(a) shows Nyquist plots of the electrodes obtained after 100 cycles at open circuit potential between 100 kHz and 10 mHz. The value of the diameter of the semicircle on the Z_{real} axis is related to the charge transfer resistance (R_{ct}). The values of R_{ct} of Sn/CNF-0.5, Sn/CNF-1, and CNF-only were 44.43, 51.58, and 90.42 Ω, respectively, representing much improved charge transport for the Sn/CNF. As indicated in Fig. 11(b), using a relationship between Z_{Re} and the square root of frequency ($\omega^{-1/2}$) in the low frequency range, the Li-ion diffusion coefficients of Sn/CNF-0.5, Sn/CNF-1, and CNF-only are determined as 5.383×10^{-14}, 5.526×10^{-13}, and 2.663×10^{-14} cm^2 s^{-1}, respectively, exhibiting much faster Li-ion diffusion process for the Sn/CNF. Thus, the improved lithium-ion reaction properties of the Sn/CNF, i.e., high specific capacity, improved stability, and excellent rate

cycling performance may be attributed to the low transport resistance and high diffusion coefficient of the lithium ion in the composite electrode consisting of Sn NPs and CNF (Fig. 12).

4. CONCLUSIONS

In summary, we demonstrated the Sn/CNF composites as an anode for high-performance LIBs using electrospinning method and calcination process. The as-prepared Sn/CNF showed Sn NPs uniformly embedded in the CNF. Compared to CNF-only, Sn/CNF exhibited high specific capacity, improved stability, and excellent high rate cycling performance. The improved electrochemical reaction properties of lithium ion such as high specific capacity and excellent rate cycling performance in Sn/CNF might be attributed to the low transport resistance and high diffusion coefficient for lithium ions compared to the CNF-only.

ACKNOWLEDGMENT
This work was supported by the Human Resources Development program of the Korea Institute of Energy Technology Evaluation and Planning (KETEP) grant funded by the Korea government Ministry of Trade, Industry and Energy (No. 20144010200660).

NOTES
The authors declare no competing financial interest.

References

1. V. Etacheri, R. Marom, R. Elazari, G. Salitra, D. Aurbach, *Energy Environ. Sci*., 4 (2011) 3243-3262.
2. K. Kang, Y. S. Meng, J. Bréger, C. P. Grey, G. Ceder, *Science*, 311 (2006) 977-980.
3. B. Guo, X. Wang, P. F. Fulvio, M. Chi, S. M. Mahurin, X. -G. Sun, S. Dai, *Adv. Mater*., 23 (2011) 4661-4666.
4. C. K. Chan, X. F. Zhang, Y. Cui, *Nano Lett.*, 8 (2008) 307-309.
5. Y. -S. Hu, R. Demir-Cakan, M. -M. Titirici, J. -O. Müller, R. Schlögl, M. Antonietti, J. Maier, *Angew. Chem. Int. Ed*., 47 (2008) 1645-1649.
6. L. Martin, H. Martineza, M. Ulldemolins, B. Pecquenard, F. L. Cras, *Solid State Ion*., 215 (2012) 36-44.
7. G. -H. An, S. -J. Kim, K. -W. Park, H. -J. Ahn, *Solid State Lett*., 3 (2014) M21-M23.
8. S. -J. Kim, H. -C. Park, M. -C. Kim, D. -M. Kim, Y. -W. Lee, K. -W. Park, *J. Power Sources*, 273 (2015) 707-715.
9. J. Qin, C. He, N. Zhao, Z. Wang, C. Shi, E. -Z. Liu, J. Li, *ACS Nano*, 8 (2014) 1728-1738.
10. Y. Xu, Q. Liu, Y. Zhu, Y. Liu, A. Langrock, M. R. Zachariah, C. Wang, *Nano Lett*., 13 (2013) 470-474.
11. M. Winter, J. O. Besenhard, *Electrochim. Acta*, 45 (1999) 31-50.
12. B. Wang, B. Luo, X. Li, L. Zhi, *Mater. Today*, 15 (2012) 544-552.
13. R. Hu, M. Zhu, H. Wang, J. Liu, O. Liuzhang, J. Zou, *Acta Mater*., 60 (2012) 4695-4703.

14. S. -I. Lee, S. Yoon, C.-M. Park, J. -M. Lee, H. Kim, D. Im, S. -G. Doo, H. -J. Sohn, *Electrochim. Acta*, 54 (2008) 364-369.
15. Y. Wang, J. Y. Lee, H. C. Zeng, *Chem. Mat*., 17 (2005) 3899-3903.
16. A. M. Chockla, M. G. Panthani, V. C. Holmberg, C. M. Hessel, D. K. Reid, T. D. Bogart, J. T. Harris, C. B. Mullins, B. A. Korgel, *J. Phys. Chem*. C, 116 (2012) 11917-11923.
17. H. Li, H. Bai, Z. Tao, J. Chen, *J. Power Sources*, 217 (2012) 102-107.
18. M. Winter, J. O. Besenhard, M. E. Spahr, P. Novák, *Adv. Mater*., 10 (1998) 725-763.
19. H. Abe, T. Murai, K. Zaghib, *J. Power Sources*, 77 (1999) 110-115.
20. E. Frackowiak, F. Béguin, *Carbon*, 40 (2002) 1775-1787.
21. Y. Yao, M. T. McDowell, I. Ryu, H. Wu, N. Liu, L. Hu, W. D. Nix, Y. Cui, *Nano Lett*., 11 (2011) 2949-2954.
22. Z. Lin, L. Ji, M. D. Woodroof, X. Zhang, *J. Power Sources*, 195 (2010) 5025-5031.
23. M. Winter, R. J. Brodd, *Chem. Rev*., 104 (2004) 4245-4269.
24. D. Li, Y. Xia, *Adv. Mater*., 16 (2004) 1151-1170.
25. B. Lu, C. Zhu, Z. Zhang, W. Lan, E. Xie, *J. Mater. Chem*., 22 (2012) 1375-1379.
26. H. Chen, J. Di, N. Wang, H. Dong, J. Wu, Y. Zhao, J. Yu, L. Jiang, *Small*, 7 (2011) 1779-1783.
27. G. -H. An, H. -J. Ahn, *J. Power Sources*, 272 (2014) 828-836.
28. D. Pan, M. Ombaba, Z. -Y. Zhou, Y. Liu, S. Chen, J. Lu, *ACS Nano*, 6 (2012) 10720-10726.
29. B. Rodríguez, I. Cameán, R. García, A. B.García, *Electrochim. Acta*, 56 (2011) 5090-5094.
30. Y. Liu, P. Liu, D. Wu, Y. Huang, Y. Tang, Y. Su, F. Zhang, X. Feng, *Chem.-Eur., J*. 21 (2015) 5617-5622.
31. Y. Yang, J. Zhang, X. Wu, Y. Fu, H. Wu, S. Guo, *J. Mater. Chem*. A, 2 (2014) 9111-9117.
32. M. Sahoo, K. P. Sreena, B. P. Vinayan, S. Ramaprabhu, *Mater. Res. Bull*., 61 (2015) 383-390.
33. L. G. Bulusheva, A. V. Okotrub, A. G. Kurenya, H. Zhang, H. Zhang, X. Chen, H. Song, *Carbon*, 49 (2011) 4013-4023.
34. X. Zhou, Z. Dai, S. Liu, J. Bao, Y. -G. Guo, *Adv. Mater*., 26 (2014) 3943-3949.
35. Z. -S. Wu, W. Ren, L. Xu, F. Li, H. -M. Cheng, *ACS Nano*, 5 (2011) 5463-5471.
36. Y. Yu, Q. Yang, D. Teng, X. Yang, S. Ryu, *Electrochem. Commun*., 12 (2010) 1187-1190.
37. G. -H. An, H. -J. Ahn, *Carbon*, 65 (2013) 87-96.
38. A. C. Ferrari, *Solid State Commun*., 143 (2007) 47-57.
39. T. Chen, L. Pan, T. A. J. Loh, D. H. C. Chua, Y. Yao, Q. Chen, D. Li, W. Qin, Z. Sun, *Dalton Trans.*, 43 (2014) 14931-14935.
40. Z. R. Ismagilov, A. E. Shalaginaa, O. Yu. Podyacheva, A. V. Ischenko, L. S. Kibis, A. I. Boronin, Y. A. Chesalov, D. I. Kochubey, A. I. Romanenko, O. B. Anikeeva, T. I. Buryakov, E. N. Tkachev, *Carbon*, 47 (2009) 1922-1929.
41. K. Xiao, Y. Liu, P. Hu, G. Yu, Y. Sun, D. Zhu, *J. Am. Chem. Soc*., 127 (2005) 8614-8617.
42. Z. Zhong, G. I. Lee, C. B. Mo, S. H. Hong, J. K. Kang, *Chem. Mat*., 19 (2007) 2918-2920.
43. H. Wang, C. Zhang, Z. Liu, L. Wang, P. Han, H. Xu, K. Zhang, S. Dong, J. Yao, G. Cui, *J. Mater. Chem.*, 21 (2011) 5430-5434.
44. X. Li, J. Liu, Y. Zhang, Y. Li, H. Liu, X. Meng, J. Yang, D. Geng, D. Wang, R. Li, X. Sun, *J. Power Sources*, 197 (2012) 238-245.
45. P. Han, Y. Yue, L. Zhang, H. Xu, Z. Liu, K. Zhang, C. Zhang, S. Dong, W. Ma, G. Cui, *Carbon*, 50 (2012) 1355-1362.
46. Y. S. Jung, K. T. Lee, J. H. Ryu, D. Im, S. M. Oh, *J. Electrochem. Soc*., 152 (2005) A1452-A1457.
47. J. Hassoun, G. Derrien, S. Panero, B. Scrosati, *Adv. Mater.*, 20 (2008) 3169-3175.